Nanoscale

PAPER

View Article Online
View Journal

Cite this: DOI: 10.1039/d5nr02385h

Tunable functional coverage of biocompatible magnesium silicate nanotubes by microwave-assisted silanization

Valeria Secchi,[a] Daniela D'Alessio,[b] Andrea Erroi,[a] Silvia Mostoni,[a] Giancarlo Capitani,[b] Alberto Calloni,[c] Gianlorenzo Bussetti,[c] Massimiliano D'Arienzo,[a] Roberto Lorenzi,[a] Keren Keinan-Adamsky,[d] Shai Rahimipour,[d] Angelo Monguzzi[a] and Marcello Campione *[b]

Received 4th June 2025,
Accepted 18th August 2025

DOI: 10.1039/d5nr02385h

rsc.li/nanoscale

The controlled synthesis of biocompatible nanomaterials with tailored composition, size, and functionalities has driven the advancement of nanomedicine, enabling the development of innovative diagnostic and therapeutic strategies. A key challenge in this field is the design of nano-objects exhibiting multiple functionalities, each dedicated to a specific diagnostic or therapeutic purpose. Among these, synthetic stoichiometric chrysotile nanotubes stand out as a highly biocompatible class of non-carbon nanotubes, already demonstrating their potential for diverse applications, including fluorescence, magnetism, singlet-oxygen generation, and scintillation. Expanding this functional versatility, we report a finely tunable approach for controlling the surface silanization using 3-aminopropyl-trimethoxysilane. This is achieved *via* a microwave-assisted synthesis, which enables mild reaction conditions and significantly reduces processing time. A comprehensive multi-technique characterization is employed to elucidate the structural and chemical features of the mineral–silane interface and the underlying reaction mechanism.

Introduction

The development of nanomedicine boosted the research on complex nanomaterials accommodating multiple functionalities aimed at implementing diagnostic and therapeutic tools while ensuring biocompatibility and reduced cytotoxicity.[1] Among geo-inspired synthetic nanomaterials, magnesium silicate nanotubes (NTs) represent the unique example of mineral (non-carbon) multiwall hollow nanotubes.[2] They are constituted by a sheet of bilayer units composed of silica-like and brucite-like bonded layers. To relax the lattice misfit between the two layers, the sheet is curled to form concentric cylinders, with the brucitic layer outwards and the silica layer inward, giving rise to a chrysotile-like crystal structure (Fig. 1).[3]

The NT morphology and physical–chemical properties demonstrated to be particularly attractive in the field of nanomedicine. The nanometric tubular shape favours a safe cellular uptake, which is the crucial step for undertaking diagnostic and therapeutic applications. Moreover, the presence of the brucitic outer layer allowed to carry out several physical–chemical modifications of the pristine system to make it particularly versatile. Indeed, the brucitic layer is densely populated by leachable Mg^{2+} ions, thus it exhibits a relatively high ζ-potential in water.[4] This characteristic can be exploited to adsorb on its surface water-soluble molecular anions through ionic self-assembly (ISA). Following this procedure, NTs were functionalized with pH-sensitive fluorescent molecules.[5,6] The notable ability of NTs to cross the blood brain barrier motivated the efforts to incorporate in its structure also a ferromagnetic functionality, generating a fluoromagnetic system serving as multimodal probe for the imaging and targeting of brain cancer.[7] Furthermore, NTs exhibit scintillating properties, being able to convert X-ray radiation into violet light. On this basis, we developed a scintillation-activated photosensitizer for the singlet oxygen production, demonstrating its efficacy in *in vitro* experiments of radio- and photo-dynamic therapy of cancer.[8,9] Moreover, by anchoring selective photosensitizers that bind Alzheimer disease (AD) associated amyloid β (Aβ), we developed a nanomedicine platform enabling the treatment of AD by a photo-dynamic therapeutic approach.[10] Recently, ferromagnetic NTs were employed to immobilize exosomes forming nanocarriers to achieve controlled delivery and localization of the system into skeletal muscles to treat

[a]*Department of Materials Science, University of Milano – Bicocca, Milano I-20125, Italy*
[b]*Department of Earth and Environmental Sciences, University of Milano – Bicocca, Milano I-20126, Italy. E-mail: marcello.campione@unimib.it*
[c]*Department of Physics, Politecnico di Milano, Milano I-20133, Italy*
[d]*Department of Chemistry, Bar-Ilan University, Ramat-Gan 5290002, Israel*

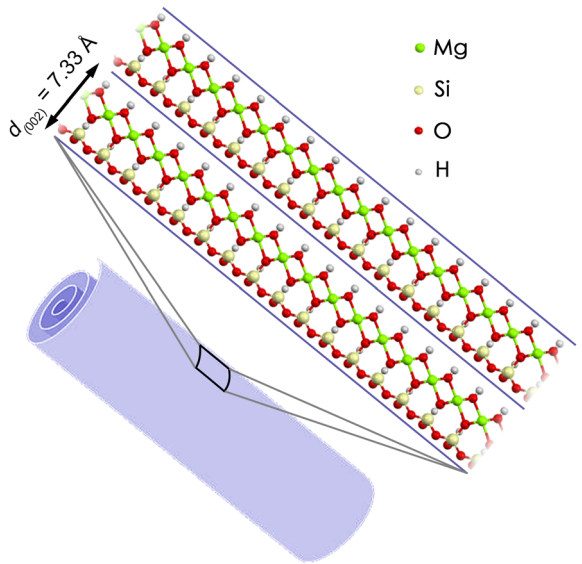

Fig. 1 Morphological and structural model of magnesium silicate NTs with chrysotile-like crystal structure. Sheets of $[Si_2O_5^{2-}]_n$ are bonded to $[Mg_3(OH)_4^{2+}]_n$ layers, to form the serpentine-like bilayer structure $Mg_3Si_2O_5(OH)_4$. The bilayer structure is rolled up on itself to form the typical multiwall hollow tubular morphology of chrysotile.

dystrophic pathologies by systemic injection using an external magnetic field.[11]

To overcome the limitations of the ISA approach to obtain a more versatile platform, the covalent grafting of the NT surface with organic molecules would represent a valuable opportunity.

Attempts aimed at grafting organic silanes on the surface of chrysotile natural fibres to improve its compatibility as filler in thermoplastics and rubber date back to 1970.[12] The authors concluded that the surface of pristine chrysotile is very unreactive to organo-silanes, and grafted derivatives can be obtained only under drastic chemical conditions and high temperature. On this basis, grafting of the chrysotile surface was realized by assisting the silanization reaction with an acidic treatment, aimed at leaching the octahedral layer to uncover silanol groups.[13–15]

Here, we present the results of the successful innovative, rapid and tunable grafting of the surface of biocompatible scintillating magnesium silicate NTs. This was achieved by the implementation of two strategies: (1) the development of a synthesis protocol for obtaining stoichiometric NTs with a controlled morphology and structure, (2) the employment of microwave (MW)-assisted methodology. Covalent attachment of silane molecules to the NTs represents a fundamental step for a stable and tunable coverage of their surface to: (i) Expand the portfolio of their functionalities by covalently attaching other molecules and producing effective multifunctional NTs for specific biological functions, such as photosensitizers necessary for X-ray-induced photodynamic therapy; (ii) improve the colloidal stability of NTs in biological environments, thus enhancing their effectiveness in biomedical applications. In this study, we chose to functionalize the NTs with 3-aminopropyl-trimethoxysilane (3-APTMS), in order to decorate the NT surface with $-NH_2$ functional groups for subsequent functionalization reactions. Our results constitute the basis for the development of multifunctional nanomaterials with finely-tunable properties having application in the field of precision and personalized medicine.

Experimental

NT synthesis

Magnesium silicate nanotubes with chrysotile-like $[Mg_3Si_2O_5(OH)_4]$ crystal structure were grown by a hydrothermal method by mixing stoichiometric quantities of sodium metasilicate nonahydrate ($Na_2SiO_3{\cdot}9H_2O$, Sigma-Aldrich) and anhydrous $MgCl_2$ (Sigma-Aldrich), in excess NaOH solution, according to the following reaction:

$$2Na_2SiO_3 + 3MgCl_2 + 2NaOH + H_2O \rightarrow Mg_3Si_2O_5(OH)_4 + 6NaCl$$

In a typical synthesis, 1520 mg of $Na_2SiO_3{\cdot}9H_2O$ are mixed with 760 mg of $MgCl_2$ and dissolved in 220 mL of NaOH 0.4 M.

The reaction was carried out in a polypropylene-lined autoclave of volume 500 mL kept at 250 °C for 16 h. The stoichiometric ratio Mg/Si influences the composition of the solid product, since it might coexist in equilibrium with brucite $[Mg(OH)_2]$ or talc $[Mg_3Si_4O_{10}(OH)_2]$ depending on the occurrence of either a deficit or an excess of the silica component, respectively.[16] The precipitate product was centrifuged and separated from the supernatant solutions. After three washing treatments with deionized water, the solid residue was exsiccated at 110 °C for 3 h. The obtainable NT amount starting from the aforementioned precursor quantities is 740 mg.

NT and brucite silanization

(40 ± 1) mg of NT or brucite (BioUltra ≥ 99%, Sigma-Aldrich) were dispersed in 5.0 mL of methanol (MeOH) in a 16 mL glass vial with the aid of a sonicating bath. Aliquots of 3-APTMS (Sigma Aldrich) 2.0% w/w solution in MeOH were added to the vial in order to form solutions with final silane weight fractions ranging from 0 to 1.0%. To study the effect of 3-APTMS concentration on NT coverage, nine different vials were prepared, each with a different concentration. Each vial was provided with a magnetic stirrer, allowing for continuous stirring during the MW treatment, and placed in a rotating PTFE rack which was inserted in a cylindric PTFE liner of 900 mL capacity, containing 150 mL of MeOH (base load) in which a temperature gauge is immersed. This liner represents the resonant chamber of the MW-reactor (SynthWave, Milestone), equipped with a 1500 W magnetron source. Thermal treatments were carried out by filling the reactor with 40 bar N_2 and starting with a linear heating ramp of 10 min from room temperature to 70 °C, followed by a dwelling stage at 70 °C for 1 h. Fig. 2 shows a representative functionalization

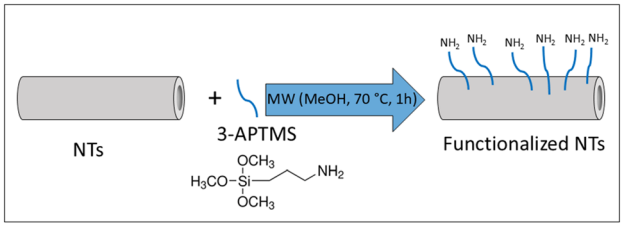

Fig. 2 Functionalization scheme: MW-assisted reaction of NTs with 3-APTMS performed for 1 h at 70 °C.

scheme adopted to decorate the NT surface with 3-APTMS. For the kinetic study, the 3-APTMS concentration was kept at 0.33%, and thermal treatments were carried out starting with a heating ramp of 10 min from room temperature to 70 °C, followed by a dwelling stage at 70 °C for times ranging from 0.5 h to 3.5 h. After the MW treatment, the contents of the vials were centrifuged and then washed one time with 15 mL of MeOH. The separated solids were dried at 70 °C for 1 h.

Characterization methods

Transmission electron microscopy and mesoporosity analysis. NTs were dispersed in isopropanol (0.25 mg mL^{-1}) and 2 μL of dispersion was deposited on lacey C-coated Cu-grids and let dry. Bright filed images were collected with a JEOL JEM 2100 Plus transmission electron microscope (TEM) operating at 200 kV.

Nitrogen physisorption analyses were performed on a BET analyzer model Autosorb-IQ-C-MP ASiQwin. Powders were outgassed at 200 °C for 24 hours before the analysis; this is a crucial step to remove any surface contaminants or adsorbed gases that could interfere with the accuracy of the analysis.

The specific surface area (SSA) was determined by the Brunauer–Emmett–Teller (BET) method, while the pore size distribution through the Barrett–Joyner–Halenda (BJH) method.

Powder X-ray diffraction. Powder X-ray diffraction (PXRD) analysis was performed with a Malvern-Panalytical X'Pert Pro powder diffractometer equipped with a Cu anode emitting Kα radiation (λ = 1.541 Å).

MicroRaman spectroscopy. Micro-Raman measurements were recorded at room temperature using a LabRAM confocal spectrometer (Horiba Jobin–Yvon) equipped with a He–Ne laser operating at 632.8 nm in backscattering configuration. The scattered light was collected by a 50× long working distance objective with a numerical aperture of 0.60 mounted on a microscope head (Olympus BX40) and detected by a charge-coupled device (CCD-Sincerity, Jobin–Yvon) with a resolution of 1 cm^{-1}. The spectral position of the detection system was calibrated with the 521 cm^{-1} Raman line of crystalline silicon as a standard.

X-ray photoemission spectroscopy. X-ray photoelectron spectroscopy (XPS) experiments were conducted using a custom-built system operating in ultra-high vacuum (base pressure < 10^{-8} Pa).[17] Photoelectrons were excited using Mg Kα radiation at $h\nu$ = 1253.6 eV and Al Kα radiation at $h\nu$ = 1486.6 eV. The emitted electrons were collected with a 150 mm hemispherical electron analyser from SPECS GmbH, operated at a pass energy of 20 eV for narrower scans, providing an overall full width at half maximum (FWHM) resolution of ~1 eV. X-ray source satellites were subtracted from the acquired spectra. Each sample was prepared by pressing NT powders onto an indium foil, which was then mounted on a sample holder before insertion into the spectrometer. To compensate for charging effects, the binding energy (BE) scale was corrected by setting the C 1s peak from aliphatic carbon contributions (C–C/C–H) at 285 eV.[18]

^{29}Si and ^{13}C cross-polarization solid-state nuclear magnetic resonance. Solid-state nuclear magnetic resonance (ssNMR) experiments were performed on a Bruker 11.7 T Avance III spectrometer using a 4 mm VTN dual channel CPMAS probe.

^{29}Si CPMAS experiments were carried out at a spinning rate of 8 kHz, using a 2.5 μs 1H 90°pulse, a cp contact time of 2 ms and a 4 s recycle delay between acquisitions.

^{13}C CPMAS experiments were carried out at a spinning rate of 8 kHz, using a 2.5 μs 1H 90°pulse, a cp contact time of 2 ms and a 3 s recycle delay between acquisitions.

Estimation of the functionalization degree. The number of 3-APTMS units grafted at the surface of NTs was determined exploiting different techniques.

Elemental analysis allows for rapid determination of carbon and nitrogen, before and after functionalization. The analysis was performed with a PerkinElmer 2400, based on the classical Pregl-Dumas method: samples are combusted in a pure oxygen environment at 800–900 °C, with the resultant combustion gases measured in an automated fashion by thermal conductivity detection.

Surface coverage of NTs with 3-APTMS was also confirmed by the ninhydrin test. A solution of ninhydrin was prepared by dissolving 0.2 g of ninhydrin in 5.0 mL of ethanol (EtOH). 500 μL of ninhydrin solution was added to each sample solution ~2 mg of NTs in 500 μL of Milli-Q H_2O or 3-APTMS in EtOH (various amounts for the calibration curve, see Fig. S1 in the SI). Samples were kept in a thermostatic box at 100° for 5 minutes to observe the colour transition and then cooled in iced water. The development of a blue/violet colour indicates the presence of NH_2 groups. 2.0 mL of EtOH solutions were added to each cuvette before the absorption measurements performed with a Varian Cary 50 spectrophotometer.

Finally, Thermo-Gravimetric Analysis (TGA) was performed by a TGA/DCS1 STARe system and allowed to determine, from the weight losses, the quantity of functionalizing agents attached to the NT surface. The analysis was performed under an air flow of 50 mL min^{-1}, over a temperature range of 30–1000 °C, with a heating rate of 10 °C min^{-1}. The temperature ramp included an isothermal step at 150 °C for 15 min to ensure complete removal of physisorbed solvent and water molecules. The calculation details for determining the quantity of bonded 3-APTMS molecules are provided in the SI (eqn (S1)–(S5)).

Results and discussion

Fig. 3 reports TEM images of NTs before (Fig. 3a, d and g) and after MW-treatment for 1 h without (Fig. 3b, e and h; blank sample) and with (Fig. 3c, f and i) 1.0% 3-APTMS. The images show clearly the tubular morphology of the synthesized particles, having average inner diameter of 6–11 nm, outer diameter of 15–25 nm, and length of 50–200 nm (Fig. 4a–c and see also Fig. S2 in the SI). At high magnification (Fig. 3g, h and i), the layered structure of NTs is revealed by the periodic contrast with spacing ~0.7 nm (Fig. 1). It is worth noting that both morphological and structural features are preserved after the MW-treatments, with and without the silanizing agent. However, the reachable resolution is not sufficient for distinguishing a possible molecular layer of 3-APTMS distributed on the surface of the NTs.

The BET-SSA and pore-size distribution of NTs were determined by nitrogen physisorption analysis. The sample shows a Type IV isotherms with a narrow hysteresis loop relatable to the presence of mesopores (Fig. 4d). The absence of a plateau at high p/p_0 is typical of aggregates. From the BET linear plot it is possible to determine a SSA value of 147 ± 3 $m^2\ g^{-1}$.

The size distribution deduced from the BJH method (Fig. 4e) results in a cumulative pore volume of 0.534 $cm^3\ g^{-1}$ and a monomodal pore size distribution cantered at ~10 nm.

From the average dimensions of NTs observed in TEM images, the available external surface and the volume of a single NT are (4–20) × 10^3 nm^2 and (25–280) × 10^3 nm^3, respectively. In principle, also the internal surface of NTs might be available for functionalization, contributing with some additional (1–7) × 10^3 nm^2. However, we note that the crystal core of chrysotile nanotubes often contains low-electron dense material, such as an amorphous phase,[3] which hinder partially or totally the entry of foreign chemical species. These inclusions derives from the growth mechanism of the NTs, being characterized by an initial stage of formation of flake-like crystallites followed by a final crystallization stage involving wrapping up of the flakes with formation of the tubular layered morphology.[19] Given the chrysotile mass density of 2.53 g cm^{-3}, we can estimate from the TEM-derived geometry

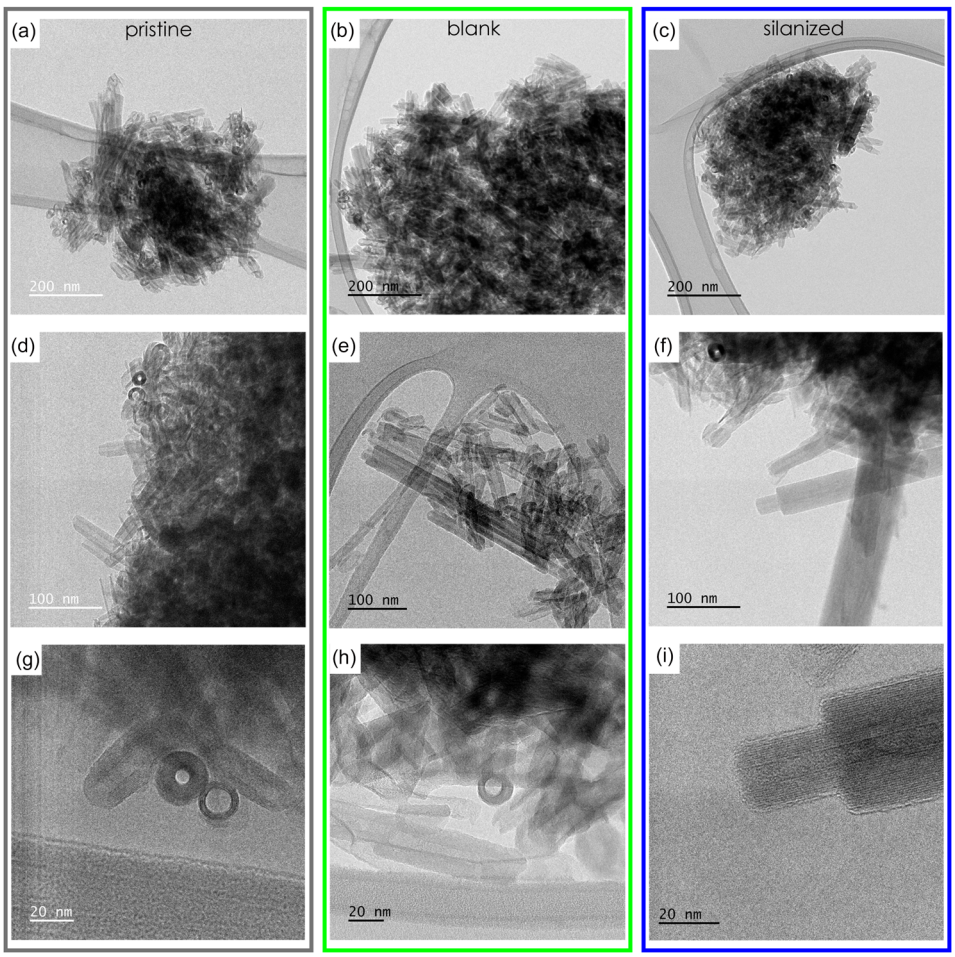

Fig. 3 Bright-filed TEM images of as synthesized NTs (a, d and g) and after MW-assisted treatment without (b, e and h) and with (c, f and i) 3-APTMS silanizing agent, deposited from isopropanol on lacey C-coated Cu-grids. The ring-like objects clearly observable in (d), (g), and (h), are NTs aligned parallel to the electron beam, whereas tubular subunits concentrically arranged in a telescopic form (cylinder-in-cylinder) are observed in panel (f) and (i).

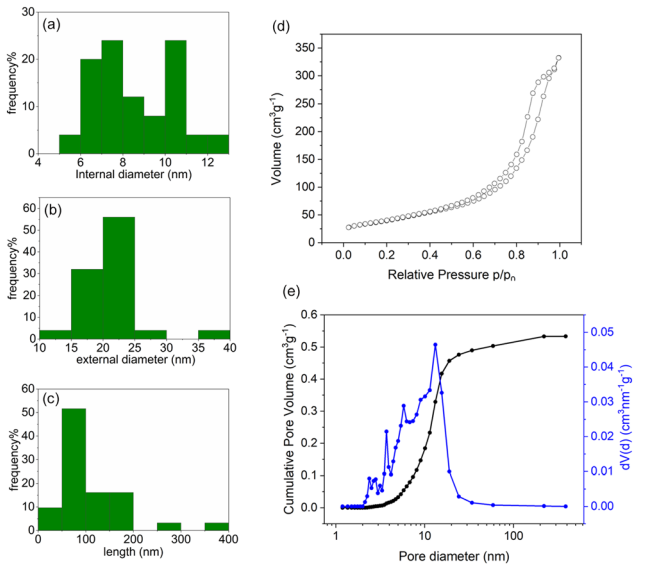

Fig. 4 (a–c) Histograms showing the size distribution of inner diameter, external diameter, and length of NTs, as deduced from the TEM images collected on pristine NTs. (d) Adsorption/desorption isotherm at liquid nitrogen temperature. (e) Pore size distribution as analyzed by the BJH method.

the average number of NTs in 1 g of sample to be 10^{16}, inferring a SSA within the range 40–200 $m^2\ g^{-1}$, which agrees with the BET estimate.

The preservation of the structure of NTs after silanization is apparent also from the diffraction patterns and Raman spectra collected on the NTs (Fig. 5a and b). Indeed, no difference is detectable among as synthesized, blank and silanized samples in PXRD experiments. All patterns show the intense small angle (002) peak given by the bilayer stacking of chrysotile (Fig. 1), together with the related (004) reflection and other bands given by the in-plane arrangement of tetrahedral and octahedral layers. Raman signals in the region 200–1150 cm^{-1} confirm that the structure is compatible with chrysotile.[20] These peaks are preserved after MW treatment and silanization. Furthermore, the presence of the CH stretching modes signals between 2800 and 3000 cm^{-1} related to the alkylic backbone of the silane molecule demonstrates the success of the silanization reaction. These peaks are evident in the spectrum of pure 3-APTMS used as a reference and are not observable in the spectrum of non-functionalized NTs.[21,22] Importantly, the silanized NTs show the presence of these peaks, however they are broader and less pronounced probably due to the formation of new bonds between the silane molecules and the NT surface.

An XPS study was conducted on the NTs to characterize their surface elemental composition and validate their preparation protocol. Fig. 6a shows the survey spectra acquired with the Mg photon source of representative samples of NTs, where features from all the expected elements are present. The line shape and peak position of N, Si, and Mg features, displayed in the narrow scans of Fig. 6b–d, is consistent with the

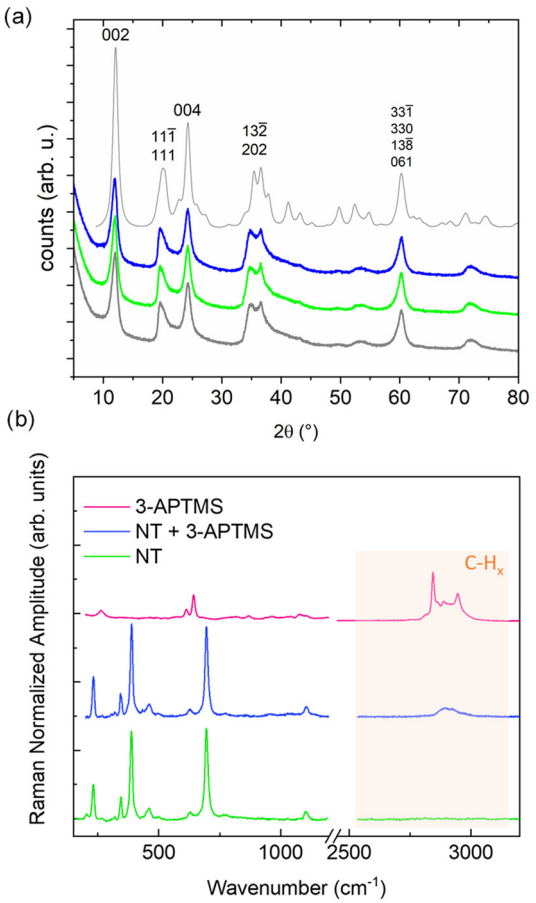

Fig. 5 (a) PXRD patterns collected on pristine NTs (grey), MeOH-treated NTs (green) and silanized NTs (blue). The pattern on top is the one simulated and indexed with the reference crystal structure of chrysotile.[3] Main diffraction bands report the miller indexes of related crystallographic planes. (b) Raman spectra of NTs (green), silanized NTs (blue) and 3-APTMS molecule as reference (pink).

literature.[4,23,24] To investigate compositional variations in the NT stratified structure without altering their composition through sputtering, we utilized an Al photon source for its greater probing depth due to the higher photon energy.[25] These additional spectra are shown in Fig. 6b–d after a proper normalization which considers the differences in the photoionization cross sections and the analysed transmission.[26,27] The visible difference in N 1s and Mg 2p intensities comparing the two excitation sources agrees with the interpretation that (N containing) silanes decorate predominantly the outermost surface of the NTs.

To study the silanization mechanism and the amount of silanes attached to the surface of the NTs, the MW-treatment was performed both on brucite samples (Table 1) and on NTs as a function of 3-APTMS concentration (S_0), starting from 0.02% (w/w) up to a maximum of 1.0% (Table 2). Established models of the crystal structure of chrysotile foresee that the outmost layer of this mineral is composed of brucite, where Mg-cations are octahedrally coordinated by OH-anions (Fig. 1). On this basis, we should expect Mg–OH groups to promote the

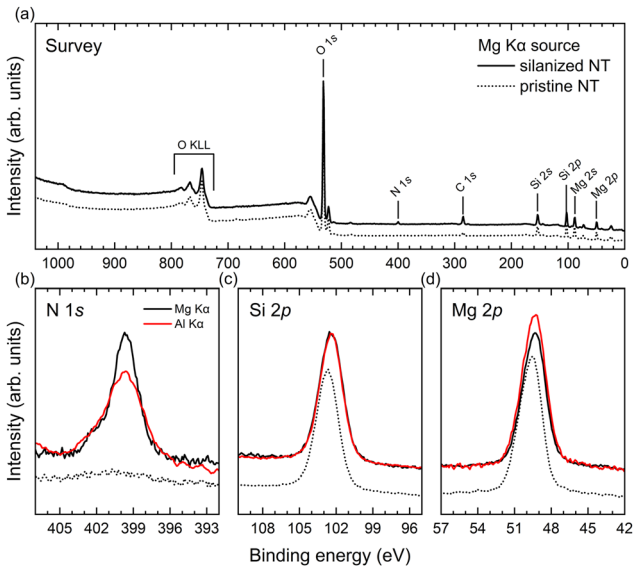

Fig. 6 Photoelectron spectroscopy results from silane-treated magnesium silicate NTs. (a) Survey scan; (b–d) narrower scans acquired in the N 1s, Si 2p and Mg 2p binding energy regions.

Table 1 Measured weight fractions of C and N in brucite samples treated with 3-APTMS

3-APTMS%	C%	N%
0.0	0.242	bdl
0.33	0.252	0.033

Table 2 Measured weight fractions of C and N and C/N ratios of NTs treated with increasing silane concentration

3-APTMS% (S_0)	C%	N%	C/N
0.0	0.470 (C_0)	0.027 (N_0)	—
0.020	0.742	0.118	2.3–8.2
0.039	1.008	0.182	3.0–6.5
0.095	1.093	0.265	2.4–4.6
0.18	1.597	0.413	2.7–4.1
0.26	1.813	0.491	2.7–3.9
0.33	1.988	0.551	2.8–3.8
0.67	2.386	0.738	2.6–3.4
1.0	2.633	0.767	2.8–3.6

bonding with silanes, with formation of Mg–O–Si bonds.[14] However, under our experimental conditions, we found that pure brucite does not react with silanes, giving rise to N% below the detection limit and C% of the order of 0.25 (Table 1). On the contrary, the C and N contents and the C/N mass ratio obtained from the elemental analysis of treated NTs (Table 2) allow to demonstrate the success of their silanization and to get an indication about the specific bond formed between the NT surface and the silane molecules.

Indeed, the attachment of 3-APTMS on NTs brings about an increment both of C- and N-atoms, which are not present in pristine NTs. These increments, and then the C/N ratio, varies

Table 3 Expected elemental fractions in 3-APTMS molecular moieties in the case of either physisorption (first row), mono- (second row), be- (third row), or tri-dentate bonding (fourth row) to a surface

3-APTMS moiety	a.m.u.	C%	H%	N%	Si%	C/N
$H_2N(CH_2)_3Si(OCH_3)_3$	179.29	40	9.0	8.0	16	5.0
$H_2N(CH_2)_3Si(OCH_3)_2-$	148.29	41	9.0	9.0	19	4.4
$H_2N(CH_2)_3Si(OCH_3)=$	117.29	41	9.0	12	24	3.4
$H_2N(CH_2)_3Si\equiv$	86.29	42	9.0	16	33	2.6

depending on the occurrence of either physisorption (first line of Table 3), mono-dentate bonding (second line of Table 3), bi-dentate bonding (third line of Table 3), or tri-dentate bonding (fourth line of Table 3).

As can be observed in Table 2, where all determinations of N- and C-atom contents of the treated NTs are listed, adventitious carbon can be present with concentrations as high as 0.47% (C_0). This, together with N% measured at null silane concentration (N_0), pose a lower and upper limit to the calculation of the C/N ratio: $C/N = [(C\% - C_0)/N\%, C\%/(N\% - N_0)]$. The C/N ranges reported in Table 2 are all consistent with the expected ones and they tend to converge to values corresponding to the formation of bi- and tri-dentate bonds (Table 3).

To corroborate this evidence, we performed ^{29}Si and ^{13}C cross polarization ssNMR measurements on silane-treated and untreated NTs. Untreated NTs present clear signals of di- and tri-silanol groups at −92.9 and −85.7 ppm in ^{29}Si-NMR, respectively (Fig. 7a). Treatment with 3-APTMS gives rise to a slight shift of the latter signal to −85.9 ppm, and the appearance of additional signals: at −66.7 ppm and −57.8, and a shoulder at −49.0 (Fig. 7b and c), which can be attributed to tri-, bi-, and mono-dentate bonding modes of 3-APTMS, respectively.[28,29] The aliphatic C-atoms of the propylic chain of 3-APTMS appear at −43.0, −24.3, −21.6, and −9.7 ppm in ^{13}C-NMR (Fig. 7d). The peak at −164.6 ppm is attributed to carboxyl groups, probably deriving from a magnesium carbonate phase.[30] This phase, being not present in the blank sample, originates from a specific action of 3-APTMS on the NT surface, triggering the combination of the $Mg(OH)_2$ component of the mineral with residual CO_2 dissolved in MeOH, with formation of an hydrated form of Mg-carbonate. The relatively high solubility of CO_2 in MeOH (about 3.5 times higher than in water at room temperature) and the high-pressure conditions adopted may favour this reaction.

Given the clear silanol signals in NMR results (Fig. 7a and b), the outermost layer of NTs can be assumed to be composed by a mixture of Mg–OH/Si–OH groups rather than a pure brucite layer, enabling the immediate formation of Si–O–Si bonds (Fig. 7c). Functionalization then proceeds *via* leaching of the brucite-like component ensuring the exposition of further silica for direct bonding with additional silane molecules.

The weight concentration of N-atoms obtained from the previous elemental analysis as a function of the silanes concentration adopted in MW treatments monotonically increases

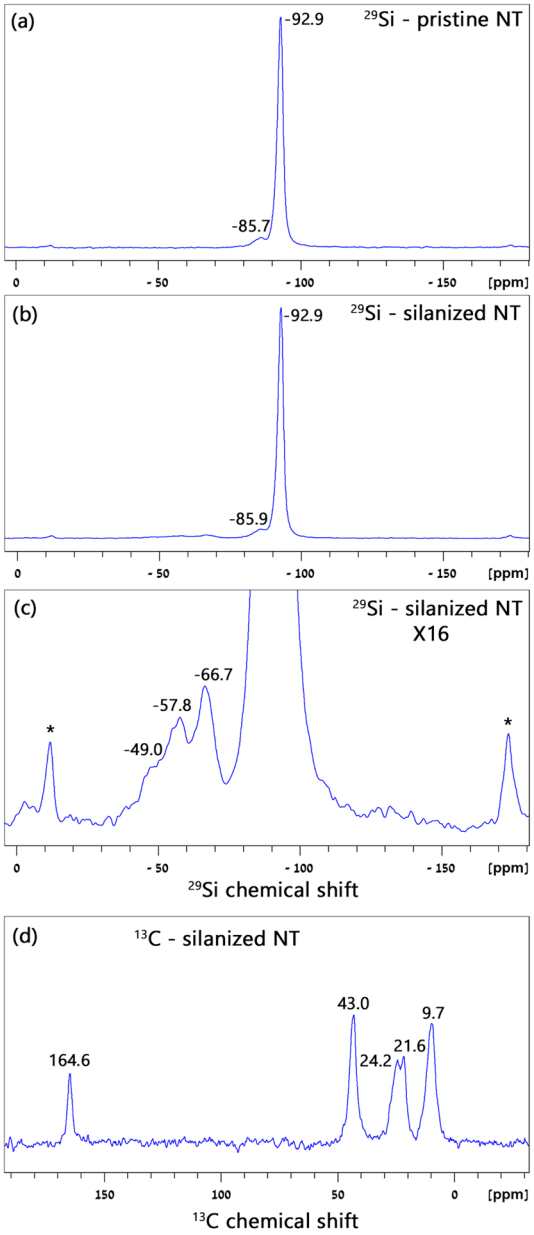

Fig. 7 NMR spectra. (a–c) ^{29}Si CP ssNMR spectrum of the (a) blank NTs and (b) the silane-saturated NTs; a spectrum with 16× expanded *y*-scale is reported in (c). The *-symbols indicate spinning sidebands. (d) ^{13}C CP ssNMR spectrum of the silane-saturated NTs.

from 0.027% (adventitious N measured in pristine NT, Table 2) for saturating at ~0.8% (Fig. 8a). The data show an apparent exponential dependence on silane initial concentration (S_0). Indeed, fitting of the data with a function of the type $N\%(S_0) = N\%_{sat}(1 - e^{-(S_0)/\gamma})$, gives $N\%_{sat} = 0.77 \pm 0.03$ and $\gamma = 0.24 \pm 0.03$, providing the best estimate of the N weight concentration at saturation ($N\%_{sat}$) and demonstrating the possibility to tune the NT surface coverage with a precision of the order of 5–10%. It is worth noting that the coverage level of the NT sample used in the characterization studies and presented in Fig. 3 and 5–7 corresponds almost to saturation (1 h-treatment with 3-APTMS 1.0%, Table 2).

In order to assess the number of bonded 3-APTMS per unit surface (σ) and per single NT (right *y*-axis in Fig. 8a), we can assume that, by neglecting the increment of mass due to the silane grafting, 1 g of functionalized NTs contain N%/100 grams of nitrogen and an average number of 10^{16} nanotube units (see the morphological characterization). Then, the number of N-atoms is calculated as $N\%\cdot 0.01\cdot N_A/14$, where N_A is the Avogadro's number and 14 is the atomic mass of *N*. Bearing only one N-atom, silane molecules have the same abundance of N-atoms. Ultimately, n.silanes per nm^2 = σ = $N\%\cdot N_A/SSA[m^2\ g^{-1}]\cdot 14 \times 10^{20}$ and n.silanes per NT = $N\%\cdot N_A/14 \times 10^{18}$. At saturation, given the estimated SSA *via* BET, σ = 2.2 nm^{-2}, whereas, as observed in Fig. 8a, the number of molecules per NT saturates at $\sim 4 \times 10^4$, which is consistent with a complete coverage of the available NT surface, with each molecule occupying an area of 0.2–0.3 nm^2.

The exponential dependence as a function of 3-APTMS concentration is confirmed by the ninhydrin test (Fig. 8b and c). This assay is based on the change in colour of the ninhydrin moiety from yellow to dark blue-purple after reaction with NH_2 groups. Fig. 8c shows the trend of the absorbance measured at λ = 588 nm of the silanized NTs as a function of the concentration of 3-APTMS normalized over the weight of samples (absorption spectra inset). From the 3-APTMS calibration curve performed by measuring the absorbance at λ = 588 nm of increasing numbers of 3-APTMS molecules (Fig. S1 in the SI) it was possible to calculate the molar extinction coefficient $\varepsilon = 9.12 \times 10^{-18}$ (cm M)$^{-1}$ as the slope of the straight line. Furthermore, using the Lambert–Beer law, we estimate that there are $\sim 1 \times 10^{17}$ silanes per mg of functionalized NTs, corresponding to $\sim 10^4$ molecules per single NT, in agreement with the results of the elemental analysis (Fig. 8a).

To further assess the possibility to finely tune the coverage of the NT surface and to get insights into the reaction kinetics, we analysed the functionalization trend as a function of the treatment time at an intermediate silane concentration of 0.33%. It must be noted that the treatment time is composed by a fixed heating stage from room temperature to 70 °C lasting 10 min, followed by a dwelling stage lasting a variable time (see Experimental section). This latter time is considered as the independent variable influencing the level of functionalization. The trend of the weight fraction of bonded N with dwelling time is reported in Fig. 9.

It is observed that, within the range 0–90 min, the N concentration increases monotonically with the tendency to reach a plateau. However, for longer times, the N concentration might decrease. This observation, also verified for other values of the starting concentration of 3-APTMS for t > 60 min, is indicative of a tendency to silane detachment and/or degradation after prolonged reaction time under MW irradiation. To corroborate this, C/N ratios (labels of experimental points in Fig. 9) are observed to be in accordance with values corresponding to di- and tri-dentate bonding, similarly to the data in Table 2. Fitting of the data was carried out assuming a

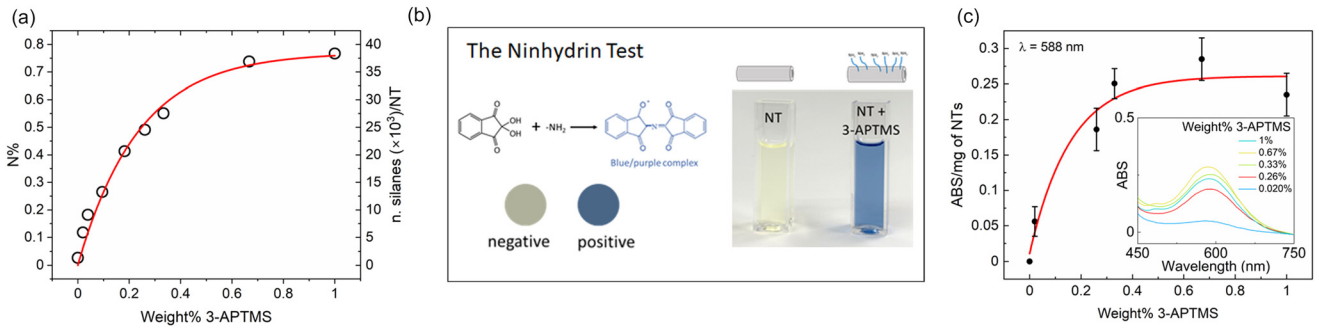

Fig. 8 (a) N% in NTs (left *y*-axis, uncertainties are within the symbol size) and estimation of the number of silane molecules per NT (right *y*-axis) as a function of the silane concentration adopted in MW treatments at 70 °C for 1 h. (b) The ninhydrin assay: a blue/violet color indicates the presence of NH_2 groups, (c) exponential dependence as a function of 3-APTMS concentration adopted in MW treatments by the ninhydrin test: the image shows the absorbance value measured at λ = 588 nm of ninhydrin solutions of silanized NTs normalized over the weight of samples. The inset shows the absorbance spectra of the silanized NTs with increasing concentration of 3-APTMS from 0.02% by weight up to a maximum of 1.0%.

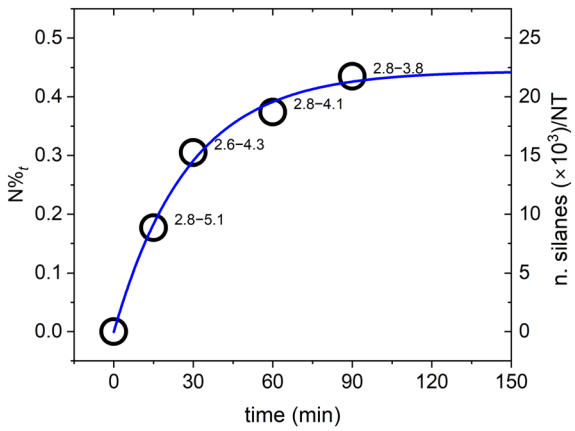

Fig. 9 N% in NTs (left *y*-axis, uncertainties are within the symbol size) and estimation of the number of silane molecules per NT (right *y*-axis) as a function of the dwelling time under MW irradiation at 70 °C with silane concentration of 0.33%. Experimental data are labelled with the measured C/N range.

Langmuir adsorption kinetics, introducing an offset ($[N\%]_0$) substantiating the possibility to reach a non-zero N concentration at dwelling time t = 0: $N\%_t = [N\%]_0 + N\%_{eq}(1 - e^{-kt})$, where $N\%_{eq}$ indicates the (S_0-dependent, Fig. 8a) equilibrium concentration of N, and k is the kinetic constant. Best-fit parameters are: $[N\%]_0 = 0.00 \pm 0.01$, $N\%_{eq} = 0.44 \pm 0.02$, and $k = (0.036 \pm 0.005)\ min^{-1} = (6.0 \pm 0.8) \times 10^{-4}\ s^{-1}$. With $N\%_{eq} = 0.44$ we infer $\sigma = 1.3\ nm^{-2}$.

TGA analysis was carried out as a countercheck of the quantity of functionalizing agent anchored to the NTs surface and to verify that the NTs are not modified by the MeOH used as solvent. Fig. S3 in the SI shows the thermal profiles of bare NTs and NTs + 3-APTMS after a reaction time of 90 min. Apart from an initial weight loss till 150 °C related to the removal of surface adsorbed water and/or solvent molecules, bare NTs (black line in Fig. S3) exhibit a significant weight loss due to dehydroxylation process starting at ~350 °C (eqn (S2) in the SI). At higher temperatures, when dehydroxylation is nearly complete, the loss of residual hydroxyl groups is responsible of the further weight decay until 750 °C.

A similar thermal profile is observed in the case of functionalized NTs (blue line in Fig. S3 in the SI). However, at temperatures above 600 °C, a slightly more pronounced weight loss is clearly detectable (see inset in Fig. S3 in the SI), which is ascribable to the surface 3-APTMS groups thermal decomposition. The 3-APTMS grafted amount (weight%) and σ was estimated according to eqn (S4) and (S5) in the SI, respectively, referring to the specific surface area of NTs determined by nitrogen physisorption analysis (SSA = 147 ± 3 $m^2\ g^{-1}$, from BET isotherm reported in Fig. 4d) under the assumption that each 3-APTMS molecule is attached *via* one, two or three hydroxyl groups. The trend of the hydroxylation degree (blank samples) and the functionalization degree as function of the reaction time for the same sample series reported in Fig. 9 are shown in Fig. S4 and S5 in the SI. The amount of hydroxyl groups is observed to have negligible variations with time, settling at a value of 26.5%, slightly higher than that corresponding to the stoichiometric fraction of water in chrysotile (24.5%). σ increases as a function of the reaction time and as expected, the highest coverage degree can be obtained under the assumption of a complete condensation reaction of 3-APTMS molecules on NTs, in which three hydroxyl groups are involved. The estimated highest value reached by σ is 1.3 nm^{-2} assuming bi-dentate bonding, and 1.9 nm^{-2} assuming tri-dentate bonding, to be compared with 1.3 nm^{-2} obtained by the elemental analysis.

Conclusions

Geomimetic NTs having the structural motif of the mineral chrysotile were synthesized and silanized using an innovative MW-assisted methodology. MW irradiation ensures a series of favourable conditions such as uniform (bulk) heating of the reaction mixture, the activation of specific chemical species and a fine control on energy and energy rate delivered to the system. By controlling the reaction time and initial concen-

tration of the silanizing agent, we showed that, with this methodology, surface coverage of the NT surface can be controlled with an uncertainty as low as 5–10% up to complete coverage. Silanization is triggered by the surface silanol groups and proceeds by removal of the brucitic layer with formation of bidentate and tri-dentate Si–O–Si bonds provided by the underlying silica layer. For a 1h-treatment, a surface coverage on 2.2 molecules per nm^2 can be reached. It should be noted that the tunability of the surface functionalization of a versatile biocompatible nanoparticle such as magnesium silicate NTs and the low reaction time and temperature required (<1 h and 70 °C, respectively), are promising elements for large-scale production of NTs having the ability to host multiple functionalities and then to expand their application in nanomedicine and related fields.

Author contributions

V. S.: data curation, formal analysis, funding acquisition, investigation, supervision, visualization, writing. D. D.: investigation, project administration. A. E.: data curation investigation. S. M.: data curation, formal analysis, investigation, visualization, writing. G. C.: data curation, investigation, methodology, resources, review & editing. A. C.: data curation, investigation, visualization, writing. G. B.: investigation, methodology, resources, writing. M. D.: investigation, methodology, resources, validation, writing. R. L.: data curation, investigation, resources, visualization, writing. K. K-A.: data curation, investigation, methodology, visualization, writing. S. R.: conceptualization, funding acquisition, methodology, validation, writing. A. M.: funding acquisition, methodology, project administration, writing. M. C.: conceptualization, data curation, formal analysis, funding acquisition, methodology, supervision, validation, visualization, writing. All the authors have approved the final manuscript.

Conflicts of interest

There are no conflicts to declare.

Data availability

The data supporting this article have been included as part of the SI: calibration of the optical absorption response of ninhydrin, TEM images of isolated NTs, TGA methodology and results. See DOI: **https://doi.org/10.1039/d5nr02385h**.

Acknowledgements

M. C. acknowledges contributions from The University of Milano – Bicocca and Cariplo Foundation (Anticarb Project) through grants no. 2024-ATEQC-0017 and 2020-0977, respectively, and thanks Fabio Moia for his help in performing the elemental analysis. A. M., R. L. and V. S. acknowledge contribution from project no. PNC0000003 – AdvaNced Technologies for Human-centrEd Medicine (project acronym: ANTHEM). A. E. thanks grant no. H45F2100343000, grant MINERVA LuMIminesceNt scintillating hEterostructures foR advanced medical imaging. V. S. and D. D. acknowledge the contributions from the University of Milano-Bicocca Starting Grant 2024-ATESP-0005.

References

1 X. Yang, L. Gao, Q. Guo, *et al.*, *Nano Res.*, 2020, **13**, 2579.
2 M. Serra, R. Arenal and R. Tenne, *Nanoscale*, 2019, **11**, 8073.
3 G. Falini, E. Foresti, M. Gazzano, A. F. Gualtieri, M. Leoni, I. G. Lesci and N. Roveri, *Chem. – Eur. J.*, 2004, **10**, 3043.
4 I. G. Lesci, G. Balducci, F. Pierini, F. Soavi and N. Roveri, *Microporous Mesoporous Mater.*, 2014, **197**, 8.
5 G. De Luca, A. Romeo, V. Villari, N. Micali, I. Foltran, I. Foresti, I. G. Lesci, N. Roveri, T. Zuccheri and L. Monsu, *J. Am. Chem. Soc.*, 2009, **131**, 6920.
6 A. Monguzzi, I. G. Lesci, G. Capitani, N. Santo, N. Roveri and M. Campione, *Phys. Chem. Chem. Phys.*, 2014, **16**, 2491.
7 C. Villa, M. Campione, B. Santiago-González, F. Alessandrini, S. Erratico, I. Zucca, M. G. Bruzzone, L. Forzenigo, P. Malatesta, M. Mauri, E. Trombetta, S. Brovelli, Y. Torrente, F. Meinardi and A. Monguzzi, *Adv. Funct. Mater.*, 2018, **28**, 1707582.
8 I. Villa, R. Crapanzano, V. Secchi, M. Tawfilas, E. Trombetta, L. Porretti, A. Brambilla, M. Campione, Y. Torrente, A. Vedda and A. Monguzzi, *ACS Appl. Mater. Interfaces*, 2021, **13**, 12997.
9 V. Secchi, F. Cova, I. Villa, V. Babin, M. Nikl, M. Campione and A. Monguzzi, *ACS Appl. Mater. Interfaces*, 2023, **15**, 24693.
10 I. Senapati, V. Secchi, F. Cova, M. Richman, I. Villa, R. Yehuda, Y. Shenberger, M. Campione, S. Rahimipour and A. Monguzzi, *Adv. Healthcare Mater.*, 2023, **197**, 2301527.
11 C. Villa, V. Secchi, M. Macchi, *et al.*, *Nat. Nanotechnol.*, 2024, **19**, 1532.
12 H. Edwards, *J. Appl. Chem.*, 1970, **20**, 76.
13 E. Mendelovici, R. L. Frost and T. Kloprogge, *J. Colloid Interface Sci.*, 2001, **238**, 273.
14 M. G. Fonseca and C. Airoldi, *J. Mater. Chem.*, 1999, **9**, 1375.
15 M. G. Fonseca, A. S. Oliveira and C. Airoldi, *J. Colloid Interface Sci.*, 2001, **240**, 533.
16 M. Campione, A. Monguzzi, B. Santiago-Gonzalez, C. Villa, Y. Torrente and M. G. Bruzzone, in *Encyclopedia of Interfacial Chemistry: Surface Science and Electrochemistry*, ed. K. Wandelt, Elsevier, Amsterdam, 2018, pp. 32–37.
17 G. Berti, A. Calloni, A. Brambilla, G. Bussetti, L. Duò and F. Ciccacci, *Rev. Sci. Instrum.*, 2014, **85**, 073901.
18 M. C. Biesinger, *Appl. Surf. Sci.*, 2022, **597**, 153681.
19 R. Lafay, A. Fernandez-Martinez, G. Montes-Hernandez, A. L. Auzende and A. Poulan, *Am. Mineral.*, 2016, **101**, 2666.

20 R. Trittschack and B. Grobéty, *Am. Mineral.*, 2013, **98**, 1133.
21 I. Shimizu, H. Okabayashi, K. Taga, A. Yoshino, E. Nishio and C. J. O'Connor, *Vib. Spectrosc.*, 1997, **60**, 125.
22 L. B. Fitaroni, T. A. Cacuro, C. A. R. Costa, E. M. Lanzoni, D. Galante, J. R. Araujo, M. G. P. Homem, W. R. Waldman and S. A. Cruz, *J. Mater. Sci.*, 2021, **56**, 9532.
23 S. Seal, S. Krezoski, D. Petering, T. L. Barr, J. Klinowski and P. Evans, *J. Vac. Sci. Technol., A*, 1996, **14**, 1770.
24 M. Gueye, T. Gies, C. Noël, S. Migot-Choux, S. Bulou, E. Lecoq, P. Choquet, K. Kutasi and T. Belmonte, *Plasma Chem. Plasma Process.*, 2016, **36**, 1031.
25 J. F. Watts and J. E. Castle, *Surf. Interface Anal.*, 2025, **56**, 408.
26 J. J. Yeh and I. Lindau, *At. Data Nucl. Data Tables*, 1985, **32**, 1.
27 L. Zommer, *Vacuum*, 1995, **46**, 617.
28 G. S. Caravajal, D. E. Leyden, V. Villari, G. R. Quintin and G. E. Maciel, *Anal. Chem.*, 1998, **60**, 1776.
29 S. Ek, E. I. Iiskola, L. Niinistö, J. Vaittinen, T. T. Pakkanen and A. Root, *J. Phys. Chem. B*, 2004, **108**, 11454.
30 J. Cui, T. R. Prisk, D. L. Olmsted, V. Su, M. Asta and S. E. Hayes, *Chem. – Eur. J.*, 1998, **29**, e202203052.